

Lensing covariance on cut sky and SPT-Planck lensing tensions

Pavel Motloch^{1,2} and Wayne Hu³

¹*Canadian Institute for Theoretical Astrophysics,
60 St. George St., Toronto, Ontario M5S 3H8, Canada*

²*Kavli Institute for Cosmological Physics, Department of Physics,
University of Chicago, Chicago, Illinois 60637, U.S.A*

³*Kavli Institute for Cosmological Physics, Department of Astronomy & Astrophysics,
Enrico Fermi Institute, University of Chicago, Chicago, Illinois 60637, U.S.A*

We investigate correlations induced by gravitational lensing on simulated cosmic microwave background data of experiments with an incomplete sky coverage and their effect on inferences from the South Pole Telescope data. These correlations agree well with the theoretical expectations, given by the sum of super-sample and intra-sample lensing terms, with only a typically negligible $\sim 5\%$ discrepancy in the amplitude of the super-sample lensing effect. Including these effects we find that lensing constraints are in 3.0σ or 2.1σ tension between the SPT polarization measurements and Planck temperature or lensing reconstruction constraints respectively. If the lensing-induced covariance effects are neglected, the significance of these tensions increases to 3.5σ or 2.5σ . Using the standard scaling parameter A_L substantially underestimates the significance of the tension once other parameters are marginalized over. By parameterizing the super-sample lensing through the mean convergence in the SPT footprint, we find a hint of underdensity in the SPT region. We also constrain extra sharpening of the CMB acoustic peaks due to missing smoothing of the peaks by super-sample lenses at a level that is much smaller than the lens sample variance. Finally, we extend the usual “shift in the means” statistic for evaluating tensions to non-Gaussian posteriors, generalize an approach to extract correlation modes from noisy simulated covariance matrices, and present a treatment of correlation modes not as data covariances but as auxiliary model parameters.

I. INTRODUCTION

Cosmic microwave background (CMB) measurements [1, 2] have been instrumental in confirming the Λ cold dark matter model (Λ CDM) as the standard model of cosmology and in constraining its parameters. Gravitational lensing of the CMB (see [3] for a review), recently measured with high significance by a number of experiments [4–14], is a secondary effect that allows us to break geometric degeneracy in the CMB data and constrain the low redshift Universe parameters, such as properties of the dark energy and the sum of neutrino masses. Upcoming CMB experiments [15–18] promise to greatly improve on these measurements and make unprecedented measurements of the low redshift physics in the linear regime.

With the increasing precision of the measurements, it is necessary to dedicate increasing scrutiny to subtle effects that have been omitted so far in most analyses. One such effect is the non-Gaussian correlations induced in the CMB data by the gravitational lensing [19, 20], reflecting the stochastic nature of the gravitational lensing potential ϕ . These correlations have been investigated on simulations for an idealized full-sky experiment [19, 21]. However, in reality all CMB experiments can only utilize the information on a portion of the sky. It is thus timely to investigate lensing-induced covariances for a cut sky experiments and check their theoretical description on simulations. Such a study is presented in the first part of this work.

Then we focus on the CMB polarization measurements from the South Pole Telescope (SPT) to better under-

stand how the lensing-induced covariance terms manifests on the cosmological parameter level and how they affect information extracted from the lensing potential. For the latter, these effects are already important for SPT data.

Lastly, while the standard cosmological model is a very good description of the experimental data, there are several tensions that can potentially signal presence of new physics [22–24]. One of the problems is an anomalously high amount of lensing detected through the smoothing of the acoustic peaks in the Planck temperature power spectra [25–27]. Using a novel technique that allows a direct comparison of gravitational lensing constraints obtained from various data sets [28, 29], it is possible to check to what extent the SPT lensing measurements agree with the lensing constraints from Planck, as we do in the final part of this work.

The outline of the paper is as follows. In § II we present our numerical simulations of lensed CMB data and study their covariances as determined by cut sky experiments. We provide several technical details as Appendices, quantifying agreement between the simulated covariance matrices and theoretical expectations of the lensing-induced covariance terms in Appendix A and constraining extra sharpening of the CMB acoustic peaks due to missing smoothing by the super-sample lenses in Appendix B. In § III we present the data sets used in this paper and discuss the details of their analysis. In § IV we conduct a case study of the effect of the lensing-induced covariance terms in the SPTpol polarization likelihood, especially in terms of how they affect cosmological parameter constraints. Finally, in § V we compare constraints on

TABLE I. Fiducial Λ CDM parameters used in this work.^a

Parameter	Fiducial value
$100 \theta_*$	1.041
$\Omega_c h^2$	0.1197
$\Omega_b h^2$	0.02223
n_s	0.9658
$\ln(10^{10} A_s)$	3.049
τ	0.058

^a In Λ CDM, these parameters also imply a Hubble constant of $h = 0.6733$.

gravitational lensing from various SPT and Planck data sets using a generalization of the standard “shift in the means” statistic, which we present in Appendix C. We conclude in § VI.

II. LENSING INDUCED COVARIANCE IN CUT SKY SIMULATIONS

In this section we describe our simulations of CMB experiments with an incomplete sky coverage and briefly summarize the standard pseudo- C_ℓ method, before we present our results on CMB power spectra covariances and compare them against theoretical expectations.

A. Simulations

To simulate lensed CMB data we use the publicly available code `Lenspix`^{*1} [30] with unlensed CMB power spectra calculated by `CAMB`^{*2} [31].

The fiducial cosmological model used to calculate the simulated CMB data is the best fit flat Λ CDM cosmological model, determined from the 2015 Planck temperature and low- ℓ polarization likelihoods assuming no primordial tensor modes and minimal mass neutrinos ($\sum m_\nu = 60$ meV). To reflect the updated results on the optical depth to recombination τ from [32], we set τ to the value from that work and decrease A_s to keep $A_s e^{-2\tau}$ constant.

The six parameters of the Λ CDM model are: $\Omega_b h^2$, the physical baryon density; $\Omega_c h^2$, the physical cold dark matter density; n_s , the tilt of the scalar power spectrum; $\ln A_s$, its log amplitude at $k = 0.05$ Mpc⁻¹; τ the optical depth through reionization, and θ_* , the angular scale of the sound horizon at recombination. Their fiducial values considered in this work are listed in Table I.

B. Pseudo- C_ℓ

In this section we briefly summarize the standard pseudo- C_ℓ approach of analyzing the cut-sky CMB data [33, 34].

The part of the sky observed by a finite survey can be described by a window function (also called mask) $w(\hat{n})$, that is zero outside of the observed region. Inside, w can be chosen to attain values between zero and one, for example to reduce ringing in the Fourier space.

Effectively, such experiments measure the fluctuations of the underlying CMB temperature T and Stokes Q and U parameters windowed,

$$\begin{aligned} T_w(\hat{n}) &= w(\hat{n})T(\hat{n}), \\ Q_w(\hat{n}) &= w(\hat{n})Q(\hat{n}), \\ U_w(\hat{n}) &= w(\hat{n})U(\hat{n}). \end{aligned} \quad (1)$$

As usual, it is possible to transfer from the masked fields (T_w, Q_w, U_w) to the spin and parity eigenstates (T_w, E_w, B_w) . Their power spectra

$$\hat{C}_{w,\ell}^{XY} = \sum_m \frac{X_{w,\ell m}^* Y_{w,\ell m}}{2\ell + 1} \quad (2)$$

are called pseudo- C_ℓ power spectra. Here we use XY, WZ to denote elements from $\{TT, TE, EE, BB\}$.

Given a statistically isotropic underlying CMB sky,

$$\langle X_{\ell' m'}^* Y_{\ell m} \rangle = \delta_{\ell\ell'} \delta_{mm'} C_\ell^{XY}, \quad (3)$$

the ensemble average of the pseudo- C_ℓ power spectra are linearly related to the power spectra of the underlying CMB C_ℓ^{XY} as

$$C_{w,\ell}^{XY} = \sum_{WZ, \ell'} M_{\ell\ell'}^{XY, WZ} C_{\ell'}^{WZ}. \quad (4)$$

Analytical expressions for the mode coupling matrices $M_{\ell\ell'}^{XY, WZ}$ can be found for example in [34]. The mask mixes E and B modes but in this work, we neglect the information in the lensed C_ℓ^{BB} spectra and focus only on the TT, TE and EE power spectra. Without C_ℓ^{BB} , $M_{\ell\ell'}^{XY, WZ}$ is diagonal in XY , so from this point forward below we use a shorthand notation $M_{\ell\ell'}^{XY}$ with XY denoting $\{TT, TE, EE\}$.

For cut-sky experiments it is not possible to invert the mode coupling matrices for every ℓ and so we bin the power spectra in ℓ as

$$C_b^{XY} = \sum_\ell P_{b\ell} C_\ell^{XY}, \quad (5)$$

using the binning operator

$$P_{b\ell} = \frac{1}{\Delta\ell_b} \times \begin{cases} \frac{\ell(\ell+1)}{2\pi}, & \text{if } \ell_b \leq \ell < \ell_{b+1}, \\ 0, & \text{otherwise} \end{cases}, \quad (6)$$

^{*1} <https://github.com/cmbant/lenspix>

^{*2} <http://camb.info>

where the minimum multipole in the first bin is $\ell_1 = 2$. Unless otherwise noted, we use fixed bin widths $\Delta\ell_b \equiv \ell_{b+1} - \ell_b = 50$ in this work. The reciprocal operator reads

$$Q_{\ell b} = \begin{cases} \frac{2\pi}{\ell(\ell+1)}, & \text{if } \ell_b \leq \ell < \ell_{b+1} \\ 0, & \text{otherwise} \end{cases}. \quad (7)$$

We do not include instrumental noise, beam or filtering in our simulations.

Under these conditions, the unbiased estimator of the underlying binned true power spectra \mathcal{C}_b is

$$\hat{\mathcal{C}}_b^{XY} = \sum_{b'\ell'} (K^{XY})_{bb'}^{-1} P_{b'\ell'} \hat{\mathcal{C}}_{w,\ell}^{XY}, \quad (8)$$

where

$$K_{bb'}^{XY} = \sum_{\ell\ell'} P_{b\ell} M_{\ell\ell'}^{XY} Q_{\ell'b'}. \quad (9)$$

For future convenience we also define the operator

$$\mathcal{U}_{b\ell}^{XY} = \sum_{b'\ell'} (K^{XY})_{bb'}^{-1} P_{b'\ell'} M_{\ell'\ell}^{XY} \quad (10)$$

that enables comparison of full sky power spectra against simulation results.

In this work we investigate five different window functions. Four of them are circular caps of sizes 150 deg^2 , 250 deg^2 , 500 deg^2 and 1000 deg^2 . The fifth is a 500 deg^2 rectangular patch of sky representing the SPTpol footprint, spanning 4 hr of right ascension, from 22 hr to 2 hr, and 15° of declination, from -65° to -50° . All window functions have been apodized by a $15'$ cosine taper to reduce ringing in Fourier space.

C. Power spectra covariance

Using 2400 simulated CMB skies from §II A and the windows from §II B, we estimate the underlying binned power spectrum $\hat{\mathcal{C}}_b^{XY}$ using (8). Note that for each simulated sky we extract an estimator for each window. These estimators are nearly independent as we place these windows in vastly separated regions of sky. For each window function, we then calculate the corresponding covariance matrix

$$\text{Cov}_{bb'}^{XY,WZ} = \langle \hat{\mathcal{C}}_b^{XY} \hat{\mathcal{C}}_{b'}^{WZ} \rangle - \langle \hat{\mathcal{C}}_b^{XY} \rangle \langle \hat{\mathcal{C}}_{b'}^{WZ} \rangle. \quad (11)$$

The correlation matrix

$$\hat{R}_{bb'}^{XY,WZ} = \frac{\text{Cov}_{bb'}^{XY,WZ}}{\sqrt{\text{Cov}_{bb}^{XY,XY} \text{Cov}_{b'b'}^{WZ,WZ}}} \quad (12)$$

obtained for the SPTpol rectangular window is shown in Fig. 1; correlation matrices derived using the other windows show qualitatively similar features.

The covariance is composed of several contributions. The diagonals in $\text{Cov}^{TT,TE}$, $\text{Cov}^{TT,EE}$ and $\text{Cov}^{TE,EE}$ are

dominated by the usual Gaussian contributions, while the anti-correlated band around the main diagonal reflects the mode couplings due to the window function. Both of these effects are present also for the unlensed CMB fields.

As has been previously argued [20], gravitational lensing by lenses larger than the survey footprint leads to coherent (de)magnification, increasing or decreasing the observed angular scales within the footprint. Its effect on the power spectra is thus largely degenerate with a change in θ_* , the angular scale of the acoustic peaks. This effect and the ensuing covariance, called super-sample covariance (SSC), can be modeled as

$$\text{Cov}_{(\text{SSC})bb'}^{XY,WZ} = \sum_{\ell\ell'} \mathcal{U}_{b\ell}^{XY} \frac{\partial \ell^2 C_\ell^{XY}}{\partial \ln \ell} \frac{\sigma_\kappa^2}{\ell^2 \ell'^2} \frac{\partial \ell'^2 C_{\ell'}^{WZ}}{\partial \ln \ell'} \mathcal{U}_{b'\ell'}^{WZ}. \quad (13)$$

Here σ_κ^2 is variance of the convergence field $\kappa = -\nabla^2 \phi/2$ in the footprint,

$$\sigma_\kappa^2 = \frac{1}{A^2} \sum_{LM} |w_{LM}|^2 \frac{L^2(L+1)^2}{4} C_L^{\phi\phi}, \quad (14)$$

where A is the sky area (in radians) covered by the survey,

$$A = \int d\hat{n} w(\hat{n}), \quad (15)$$

and w_{LM} are the spherical harmonic coefficients of the window function. The factors \mathcal{U} are added on top of the standard expression from [20] to represent effects of the window function and the subsequent de-biasing. We find that in the simulated covariances, SSC is the dominant effect induced by the gravitational lensing and corresponds to the checkerboard pattern visible in Fig. 1 (see also Fig. 12 in Appendix A 2).

Finally, fluctuations of lenses within the observed footprint also correlate CMB data [19] and the intra-sample lensing covariance (ILC) they induce is given by

$$\begin{aligned} \text{Cov}_{(\text{ILC})bb'}^{XY,WZ} & \quad (16) \\ &= \frac{4\pi}{A} \sum_{L\ell\ell'} \mathcal{U}_{b\ell}^{XY} \left[\frac{\partial C_\ell^{XY}}{\partial C_L^{\phi\phi}} \frac{2(C_L^{\phi\phi})^2}{(2L+1)} \frac{\partial C_{\ell'}^{WZ}}{\partial C_L^{\phi\phi}} \right] \mathcal{U}_{b'\ell'}^{WZ}. \end{aligned}$$

It represents the correlation caused by the common dependence of the CMB power spectra on the stochastic lensing power. The inverse proportionality to the sky area A reflects the fact that due to a smaller number of measured modes, lensing power shows larger sample variance on smaller patches.

In Fig. 1 (right panel) we show the expected contribution of the lensing-induced terms, given by the sum of the SSC (13) and ILC (16) contributions, to the correlation matrix for the rectangular window function,

$$R_{(\text{theory})bb'}^{XY,WZ} = \frac{\text{Cov}_{(\text{ILC})bb'}^{XY,WZ} + \text{Cov}_{(\text{SSC})bb'}^{XY,WZ}}{\sqrt{\text{Cov}_{bb}^{XY,XY} \text{Cov}_{b'b'}^{WZ,WZ}}}. \quad (17)$$

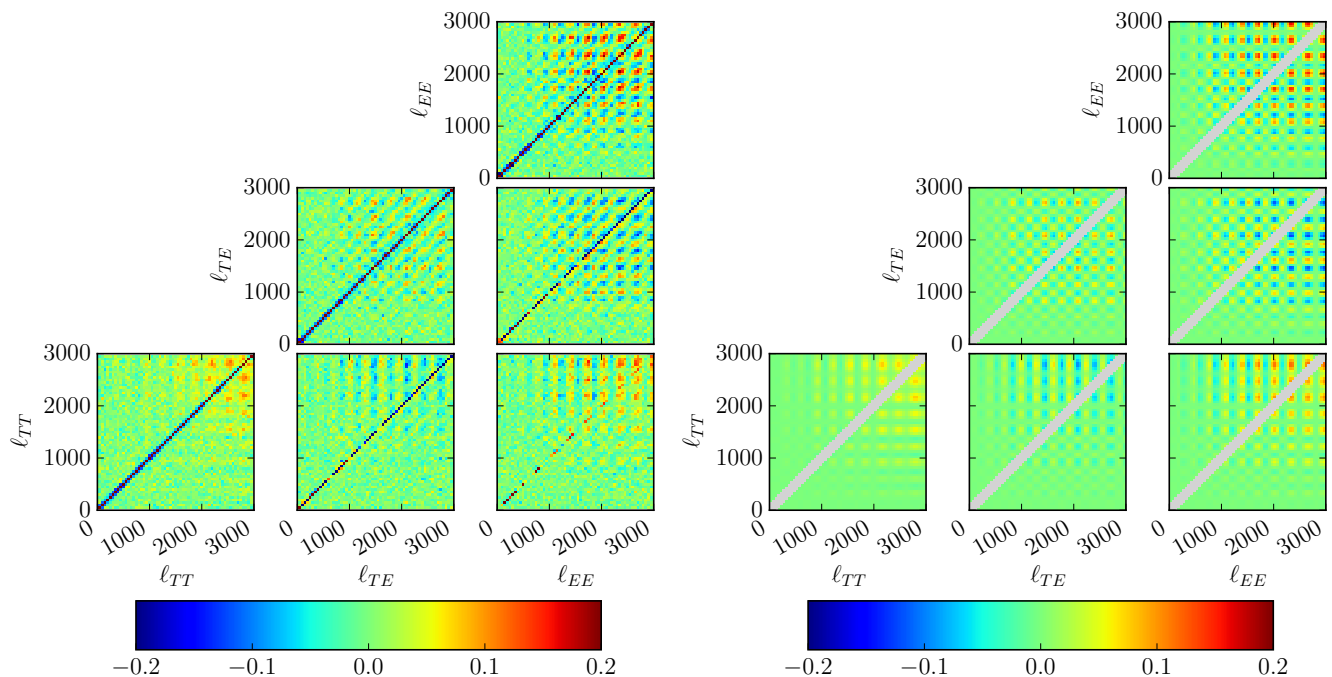


FIG. 1. Left: Correlation matrix of the unbiased estimates of the binned power spectra \hat{C}_b^{XY} calculated from the simulations with the rectangular SPT-like window function. Right: Theoretical expectation for the lensing-induced contributions to the correlation matrix, $R_{(\text{theory})bb'}^{XY,WZ}$, given by the sum of the SSC (13) and ILC (16) contributions. The gray region hides elements dominated by the Gaussian terms and the window function effects.

Notice we divide by the full covariance obtained from the simulations, as we do not model the Gaussian terms explicitly and focus only on the lensing-induced terms away from the diagonal.

In Appendix A we quantify the agreement between the lensing-induced effects in the simulated covariance matrices $\text{Cov}_{bb'}^{XY,WZ}$ and their theoretical expectations. Using template fitting, in Appendix A 1 we find that theoretical expectations match the simulations reasonably well, with the amplitude of the SSC term underestimated in the model by about $\sim 5\%$. In Appendix A 2 we introduce an alternative quantification approach, based on an idea presented in [35]. This method gives consistent results with the template fitting estimation.

Finally, in cut-sky experiments we expect to see slightly sharper acoustic peaks than in a full sky experiment. As explained above, gravitational lenses larger than the footprint lead to a coherent shift of the angular scale. A full sky experiment contains many lenses of such size, some of them locally magnifying while some of them locally demagnifying the CMB fields. Averaging over all of these lenses then leads to smoothing of the peaks. Because a cut sky experiment observes only one such lens, this averaging does not happen and we in principle expect sharper peaks. In Appendix B we investigate this effect on simulations and find that for the windows that we consider it is negligible even for cosmic variance limited CMB experiments.

III. MCMC ANALYSIS DETAILS

In this section we provide details about the Markov Chain Monte Carlo (MCMC) analyses we perform to find constraints of gravitational lensing from several data sets. We start by summarizing the data used in this paper, after which we introduce the technique used to obtain direct measurements of the gravitational lensing potential from the CMB data. We conclude with a few technical details about sampling of the posterior probability distribution.

A. Data

We compare SPT lensing constraints with those from the Planck satellite^{*3}, derived from their 2018 gravitational lensing reconstruction likelihood (Planck PP) [14] and the 2015 temperature likelihood (Planck TT) [36]. As Planck TT is not able to measure the optical depth through reionization τ , we supplement it with a Gaussian prior on τ centered on 0.058 and with width 0.02 [32]. We do not use the latest Planck parameter values [37] that were not available at the inception of this work;

^{*3} <http://pla.esac.esa.int/pla/>

we checked that the tensions between the data sets discussed in § V are insensitive to the details of the τ prior (see also [38]).

We use the publicly available SPT likelihoods^{*4}: the SPT-SZ measurement of C_ℓ^{TT} from 2500 deg² of the sky [8], lensing reconstruction likelihood based on the same data combined with the Planck temperature measurement [39] and the SPTpol measurements of C_ℓ^{TE} and C_ℓ^{EE} in a 500 deg² patch [40]. Below, we denote these likelihoods as SPT TT, SPT PP and SPT TEEE. We supplement SPT TT and SPT TEEE with the same τ prior that we use for Planck TT.

In the sections below we show that lensing-induced covariance effects, discussed in the previous section, are important enough to affect results derived from the SPT polarization measurements. In § IV we discuss ways how to modify the SPT TEEE likelihood to properly include these effects.

B. Parameterizing lensing

Here we provide a brief review of a technique to directly constrain the gravitational lensing potential from the CMB power spectra introduced in [28, 29].

The gravitational lensing potential power spectrum is parameterized in terms of N_{pc} effective parameters $\Theta^{(i)}$ which determine arbitrary variations around a fixed fiducial power spectrum $C_{L,\text{fid}}^{\phi\phi}$ as

$$C_L^{\phi\phi} = C_{L,\text{fid}}^{\phi\phi} \exp\left(\sum_{i=1}^{N_{\text{pc}}} K_L^{(i)} \Theta^{(i)}\right). \quad (18)$$

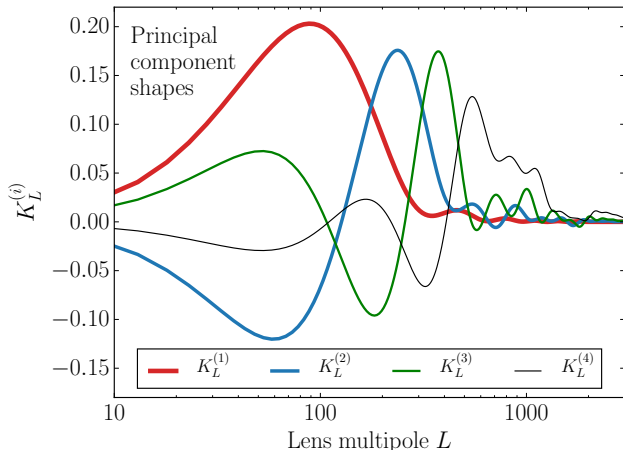


FIG. 2. Lensing principal components $K_L^{(i)}$ used in this work.

In this setup, constraining $\Theta^{(i)}$ from the data corresponds directly to constraining the gravitational lensing potential. This should be contrasted with the common approach of introducing a phenomenological parameter A_L which multiplies $C_L^{\phi\phi}$ at each point in the model space and cannot be so interpreted once model parameters are marginalized over.

We choose the same fiducial model and $K_L^{(i)}$ as in [38] to allow easier comparison to those results. More details about the fiducial model and values of cosmological parameters are given in § II A. These $K_L^{(i)}$ are chosen such that $\Theta^{(i)}$ correspond to N_{pc} principal components (PCs) of the gravitational lensing potential best measured by Planck TT, as determined using a Fisher matrix construction [38]. The resultant eigenmodes $K_L^{(i)}$ are shown in Fig. 2. We retain $N_{\text{pc}} = 4$ PCs in order to fully characterize all sources of lensing information [38]. Accommodating the PCs to the SPT covariance is not necessary, as the shapes $K_L^{(1)}$ that would correspond to the lensing modes best constrained by the SPT TT and SPT TEEE likelihoods are very close to the one derived from the Planck TT likelihood (Fig. 3). Additionally, the other principal components in SPT have variance at least ~ 100 times larger than the leading PC and the data are thus unable to constrain them strongly. Throughout this work we consistently use a single set of $K_L^{(i)}$, given by Planck TT.

In models beyond Λ CDM, changes in the integrated Sachs-Wolfe (ISW) effect would typically affect data on the largest scales. In this work we are interested only in lensing-like effects and leave the ISW contribution at its Λ CDM value.

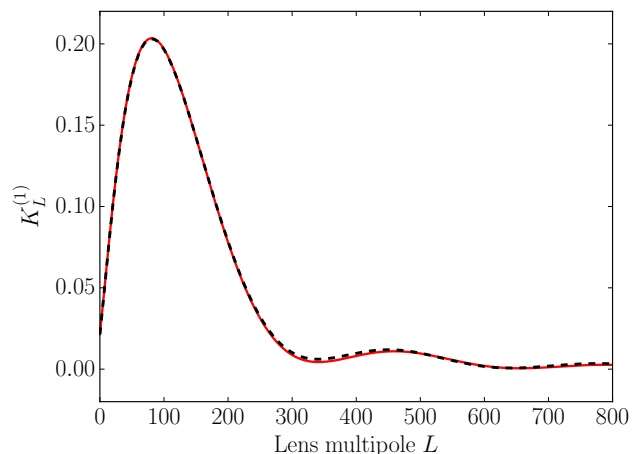


FIG. 3. Comparison of the shapes of the best measured principal component $K_L^{(1)}$ as determined from the Planck TT (black dashed) and SPT TEEE (red) data. They are very close, as is the one determined from SPT TT (not shown).

^{*4} <https://lambda.gsfc.nasa.gov/product/spt/>

C. Markov Chain Monte Carlo sampling

To sample the posterior probability in the various parameter spaces we use the MCMC code CosmoMC^{*5} [41]. Each of our chains has a sufficient number of samples such that the Gelman-Rubin statistic $R - 1$ [42] falls below 0.01.

We choose flat tophat priors on $\Theta^{(i)}$. As $\Theta^{(1)}$ is the variable in which we will evaluate the tensions between data sets, we choose uninformative prior on it. For the remaining three $\Theta^{(i)}$, that allow freedom in the shape of the gravitational lensing potential, we limit their variation such that all $C_L^{\phi\phi}$ are within a factor of 1.5 of $C_{L,\text{fid}}^{\phi\phi}$. These weak priors are meant to eliminate cases that would be in conflict with other measurements of large scale structure or imply unphysically large amplitude high frequency features in $C_L^{\phi\phi}$.

In analyses that use Planck TT, SPT TEEE or SPT TT, in addition to these four lensing parameters we also vary the six Λ CDM parameters, with flat uninformative priors. Unlike the standard analysis, which we also conduct for comparison, these only affect the unlensed power spectra and their changes do not in any way affect the gravitational lensing potential that is fully determined by $\Theta^{(i)}$ (18).

We use default foreground and nuisance parameters and their priors in all the likelihoods.

IV. LENSING COVARIANCE EFFECTS IN SPT TEEE DATA

As we will see shortly, gravitational lensing measurements from SPT TEEE are so constraining that the lensing-induced covariance terms have to be included. In this section we comment on possible ways to account for this covariance in the likelihood and what cosmological parameters are affected in the standard Λ CDM model and in its parameterized lensing extension.

A. Super-sample covariance

To obtain the data covariance matrix, the SPT collaboration used simulations based on Gaussian realizations of lensed CMB power spectra instead of actually lensing the simulated CMB data. As a consequence, in this approach the lensing-induced covariance terms are missing from their covariance matrix.

Instead of explicitly including the SSC term in the covariance matrix, the SPT collaboration introduced a new parameter $\bar{\kappa}$ into the SPT TEEE likelihood. The parameter $\bar{\kappa}$ quantifies the unknown value of the mean lensing

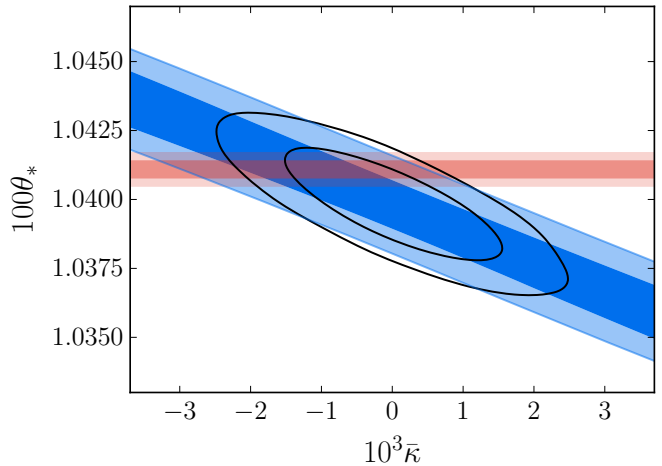


FIG. 4. Constraints on θ_* and $\bar{\kappa}$ from SPT TEEE when no prior on $\bar{\kappa}$ is chosen (blue solid) and with the $\sigma_{\bar{\kappa}} = 10^{-3}$ prior (black lines). In red we show constraints on θ_* from Planck 2018 temperature and polarization cosmological parameter constraints [37]. Results assume Λ CDM and display 68% and 95% confidence limits.

convergence in the survey which shifts the power spectra according to

$$C_\ell^{XY}(p_\mu, \bar{\kappa}) = C_\ell^{XY}(p_\mu) + \frac{\partial \ell^2 C_\ell^{XY}}{\partial \ln \ell} \frac{\bar{\kappa}}{\ell^2}, \quad (19)$$

where p_μ are the cosmological parameters.^{*6} We find that including super-sample lensing as an additional covariance by adding (13) or through the additional parameter $\bar{\kappa}$ leads to identical results. Since the measurement of $\bar{\kappa}$ can be useful when comparing to other data sets, as we show below, from this point forward we adopt it in our analysis. When considering the SSC effect we also include the ILC covariance in the analysis and vice versa, but the results are not sensitive to its inclusion.

Due to the strong degeneracy with θ_* (see Fig. 4), the parameter $\bar{\kappa}$ is only very poorly constrained by the SPT data itself and is limited by a Gaussian prior with width $\sigma_{\bar{\kappa}} = 1.0 \times 10^{-3}$, reflecting the expected fluctuations of the super-sample lenses. The size of the prior was chosen by the SPT collaboration according to (14); using our fiducial cosmology and SPTpol-like rectangular window we obtain a similar value. With $\bar{\kappa}$ prior, θ_* can be constrained, as evident from Fig. 4. The cosmological parameters other than θ_* are not significantly affected by the super-sample lensing effect.

Using SPT TEEE and assuming Λ CDM, the prior uncertainty on $\bar{\kappa}$ limits the measurement of the angular scale of the angular peaks to $100\theta_* = 1.03982 \pm 0.00135$.^{*7} For

^{*5} <https://github.com/cmbant/CosmoMC>

^{*6} This technique was introduced in [20] but note that $\bar{\kappa} \rightarrow -\bar{\kappa}$ in their Eq. (32).

^{*7} In § II C we found that variance of $\bar{\kappa}$ calculated by (14) appears

the 2018 Planck temperature and polarization data [37], the impact of SSC is negligible which allows an extremely precise measurement of θ_* : $100\theta_* = 1.04109 \pm 0.00030$, with a difference in mean from the SPT TEEE measurement that is in good agreement at 0.9σ . If SSC were ignored in the SPT TEEE analysis, constraints on the angular scale of the acoustic peaks would be too optimistic, $100\theta_* = 1.03985 \pm 0.00085$, leading to an overly significant 1.4σ difference in means.

The benefit of considering $\bar{\kappa}$ as a parameter is that when combined with the Planck 2018 measurement of θ_* , a more precise measurement of its value in the SPT field can be extracted and compared to other measurements of lensing. The Planck measurement breaks the $\bar{\kappa} - \theta_*$ degeneracy in the SPT TEEE without any need for the $\sigma_{\bar{\kappa}}$ prior. This approach allows us to determine $\bar{\kappa}$ in the SPTpol field and leads to

$$\bar{\kappa}_{\text{SPTpol}} = (-1.3 \pm 0.9) \times 10^{-3}. \quad (20)$$

The mean in the field is consistent with the expected root mean squared (rms) $\sigma_{\bar{\kappa}}$ of the Λ CDM model and the errors approach the intrinsic sensitivity of the SPT TEEE data to a fractional shift in angular scale in the absence of the $\bar{\kappa} - \theta_*$ degeneracy, i.e. $\sigma_{\theta_*}/\theta_* \approx 0.8 \times 10^{-3}$. Combined they show a mildly significant indication of an underdensity in the SPTpol footprint.

In principle, this mild preference can be tested against other measurements of lensing, for example the Planck lensing map [11]. However, the Planck lensing map is noisy and band limited to $L \geq 8$, which removes part of the super-sample lensing signal. The quantity

$$\bar{\kappa}_{\text{SPTpol}}^{\text{est}} = \frac{1}{A} \int d\hat{n} w(\hat{n}) \hat{\kappa}(\hat{n}), \quad (21)$$

where $\hat{\kappa}$ is the Planck lensing map, is an unbiased estimator of $\bar{\kappa}_{\text{SPTpol}}$ with variance

$$\sigma_{\bar{\kappa}_{\text{SPTpol}}^{\text{est}}}^2 = \frac{1}{A^2} \sum_{LM} |w_{LM}|^2 \frac{L^2(L+1)^2}{4} \chi_L^{\phi\phi}, \quad (22)$$

where

$$\chi_L^{\phi\phi} = \begin{cases} C_L^{\phi\phi}, & L < 8 \\ N_L^{\phi\phi}, & L \geq 8 \end{cases},$$

with $N_L^{\phi\phi}$ being the noise power in the Planck lensing map. The $L < 8$ terms account for the missing large scale lensing modes, while the $L \geq 8$ terms include the uncertainty due to the noise in the Planck lensing map; we assume the noise is uncorrelated with the lensing signal. Using our rectangular window function as a proxy for the real SPTpol mask, we obtain

$$\bar{\kappa}_{\text{SPTpol}}^{\text{est}} = (-0.7 \pm 1.2) \times 10^{-3}, \quad (23)$$

to be underestimated by $\sim 5\%$. Even if this is the case, the uncertainty on θ_* from SPT TEEE would grow only marginally, to 1.38×10^{-5} .

result consistent with the SPT TEEE measurements.

We see from (14) that the expectation for the rms $\bar{\kappa}$, $\sigma_{\bar{\kappa}}$, depends on the gravitational lensing potential and the SSC amplitude should in principle be evaluated in each point in the parameter space. However, in the Λ CDM model the shape and amplitude of lensing is sufficiently well constrained and consistent between measurements that parameter uncertainties provide only small changes in its value compared with the measurement errors. We shall see that the same is not true of the parameterized lensing extension to Λ CDM and so we choose not to repeat the SSC analysis of this section for this model until such tensions are resolved. Likewise, although as we shall see ILC can also be treated with auxiliary parameters, because of these tensions we do not conduct such an analysis in this work.

B. Intra-sample lensing covariance

As pointed out in the previous section, the SPT TEEE covariance is based on simulations without actual gravitational lensing and is thus missing the ILC term. To include the ILC, we add $\text{Cov}_{(\text{ILC})bb'}^{XY,WZ}$ calculated according to (16) on top of the covariance matrix provided by the SPT collaboration in the SPT TEEE likelihood. To calculate the ILC term here, we use the \mathcal{U}_{bl}^{XY} that are also provided in the SPT TEEE likelihood.

In Λ CDM, we find that the main effect of adding the intra-sample lensing covariance to SPT TEEE is a degradation of the $\Omega_c h^2$ constraints by $\sim 7\%$. This is because part of the information on $\Omega_c h^2$ comes from the smoothing of the peaks due to lensing and hence quantifying the errors on lensing information is important for its determination. Correspondingly, the constraints on the Hubble constant change from $H_0 = (70.8 \pm 2.1)$ km/s/Mpc to (70.4 ± 2.3) km/s/Mpc.

This impact on lensing information of the ILC can be best understood within the context of the model where the gravitational lensing is separately parameterized in terms of the lensing PCs $\Theta^{(i)}$. In Fig. 5 we compare constraints on the best measured PC $\Theta^{(1)}$ before and after addition of the ILC effect into the covariance. As expected, adding ILC degrades the constraints, as we are effectively adding uncertainty related to the unknown lens fluctuations. In Λ CDM, gravitational lensing information is mainly used to constrain $\Omega_c h^2$, which explains the observed effect. In extensions that change the low-redshift physics, such as by allowing the mass of the neutrinos $\sum m_\nu$ or equation of state of the dark energy parameter w to vary, the ILC most affects constraints on combinations of the Λ CDM and extension parameters that are limited by the lensing information, see [29] for a related discussion.

As evident from (16), the magnitude of the ILC effect grows with increasing gravitational lensing power. For SPT TEEE this dependence must be considered, because the constraints on gravitational lensing from SPT TEEE,

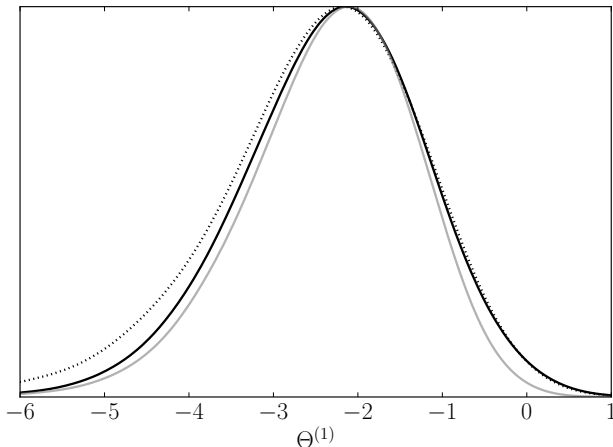


FIG. 5. Comparison of $\Theta^{(1)}$ posterior probability distributions from SPT TEEE for various models of the ILC effect: original likelihood without ILC (gray), constant ILC evaluated at the fiducial model (dotted) and $\Theta^{(1)}$ -dependent ILC (black solid).

shown in Fig. 5, are still rather weak. To partially account for this effect, we explicitly model the dependence of $\text{Cov}_{(\text{ILC})}^{XY,WZ}$ on the dominant lensing component $\Theta^{(1)}$: we evaluate (16) for a representative set of gravitational lensing potentials corresponding to $\Theta^{(1)}$ in the range constrained by SPT TEEE (see Fig. 5). We then interpolate to get a smooth dependence on $\Theta^{(1)}$ of the ILC contribution to the covariance matrix and reevaluate the covariance matrix in each point in the parameter space.

The main effect of considering the $\Theta^{(1)}$ -dependence in ILC, as opposed to using ILC evaluated for the fiducial lensing potential $C_{\text{fid},L}^{\phi\phi}$, is a suppressed probability of low values of $\Theta^{(1)}$ (Fig 5). This can be easily understood, as lower values of $\Theta^{(1)}$ correspond to smaller lensing power, leading to smaller amplitude of the ILC effect; the constraints at low $\Theta^{(1)}$ then effectively approach the case without ILC. From this point forward we use this model of ILC for the SPT TEEE analysis.

The addition of lensing-induced covariance to either of the PP likelihoods is not necessary, as the lens variance is already included in the Gaussian terms of their covariance matrices. Furthermore, due to the larger sky coverage and correspondingly smaller lens variance (recall the A^{-1} factor in (16)) and the fact that C_{ℓ}^{TT} is less sensitive to lensing effects than the polarization power spectra, ILC modifications are not necessary for the Planck TT and SPT TT likelihoods.

As a rule of thumb, the ILC effect has to be included when the $\Theta^{(1)}$ constraint from the given data set approaches

$$\sigma_{\Theta^{(1)}}^A \approx 0.048 \sqrt{\frac{4\pi}{A}}, \quad (24)$$

which is the limiting error due to the sample variance of $\Theta^{(1)}$ in a given patch of the sky.

Finally, given that future experiments will have to include the ILC effect into their analysis but will also provide much tighter constraints on lensing effects as they approach this sample variance limit, we conclude with a simple approach to incorporating the ILC effect for the purpose of cosmological parameter estimation. In this context $\text{Cov}_{(\text{ILC})bb'}^{XY,WZ}$ can be considered constant and given by the best fit parameters. The addition of ILC to the analysis can then be done in a way that parallels the treatment of SSC through $\bar{\kappa}$ by considering $\bar{\Theta}^{(i)}$ as parameters that describe a local fluctuation in the lens power spectra within the survey footprint, affecting the CMB power spectra as

$$C_{\ell}^{XY}(p_{\mu}, \bar{\Theta}^{(i)}) = C_{\ell}^{XY}(p_{\mu}) + \sum_i \frac{\partial C_{\ell}^{XY}}{\partial \bar{\Theta}^{(i)}} \bar{\Theta}^{(i)}. \quad (25)$$

Here p_{μ} are the cosmological parameters of the model and the sum is over a sufficient number of principal components, either constructed from a Fisher matrix for the experiment as we have done here for Planck or by empirically discovering them from simulations as described in Appendix A 2. To account for the effect of ILC on cosmological parameter estimation, one then marginalizes over $\bar{\Theta}^{(i)}$ given a theoretical prior on the amplitude of the lens fluctuations within the window. Note however that this procedure assumes that there is a consistent cosmological model that describes all lensing effects in all datasets, which is not currently the case, as we shall see next.

V. SPT-PLANCK LENSING TENSIONS

In this section we compare lensing constraints from the various SPT and Planck data sets using the techniques developed in the previous sections. In Fig. 6 we compare lensing constraints from all five data sets investigated in this work, including the SPT TEEE data set with a $\Theta^{(1)}$ -dependent covariance matrix.

All lensing constraints from SPT are mutually consistent, while the Planck and SPT constraints seem to be systematically offset, with SPT preferring lower values of the lensing potential (see [39, 40] for related studies). This difference corresponds to sharper acoustic peaks in the SPT data compared to Planck data. Sharper peaks cannot be caused by missing contributions from the super-sample lenses in the smaller SPT sky area (see Appendix B).

To quantify the significance of the tensions, we use a generalization to non-Gaussian distributions of the commonly used “shift in the means” statistic; this generalization is described in the Appendix C. In this work we assume all the measurements are independent.

Resulting tension significances are listed in Fig. 7. The Planck TT constraint is in over 2σ tension with all the other lensing constraints; its tension with SPT TEEE

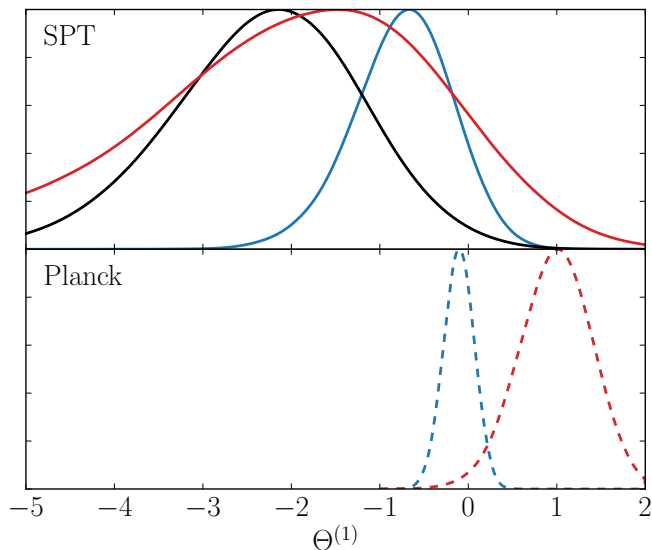


FIG. 6. Constraints on $\Theta^{(1)}$ from SPT (top) and Planck (bottom, dashed): in blue, lensing constraints from lensing reconstruction (SPT PP and Planck PP); in red, from temperature power spectra (SPT TT and Planck TT); in black, from SPT TEEE with the ILC effect included (black solid).



FIG. 7. Significance of the tensions between constraints on $\Theta^{(1)}$ from various datasets. The numbers represent tensions in the units of Gaussian standard deviations σ , so 1.0 in this table corresponds to 31.7% chance probability to exceed.

reaching 3.0σ level. The constraint from this SPT likelihood is also in a moderate 2.1σ tension with the Planck lensing reconstruction constraint.

Had we not included the ILC effect into the covariance matrix, as was the case with previous analyses, the tensions between SPT TEEE and Planck TT or Planck PP would noticeably increase from 3.0σ to 3.5σ and from 2.1σ to 2.5σ respectively. Including the dependence of ILC on $\Theta^{(1)}$ is responsible for approximately 0.05σ of the decrease. Finally, let us point out that had we used the

2015 Planck lensing likelihood instead of the 2018 update, the tension with SPT TEEE would increase by additional 0.05σ .

Tension between SPT TEEE and Planck TT was investigated using the standard A_L parameter in [40]. By comparing the SPTpol constraint $A_L = 0.81 \pm 0.14$ with the Planck temperature constraints $A_L = 1.22 \pm 0.10$, the difference in means is in 2.4σ tension^{*8}. This is significantly less than the value 3.5σ we find when not including the ILC effect and clearly shows that comparison of A_L is suboptimal, due to the fact that each A_L scales the lens potential of a different cosmological model, i.e. those preferred by SPT and Planck respectively. We checked explicitly that when one considers the full seven-parameter posterior of the Λ CDM+ A_L model, SPT TEEE and Planck TT constraints on one particular linear combination of these seven parameters disagree at the 3.5σ level. The tension is thus in principle discoverable also in the standard approach using A_L , but it is hidden in a combinations of parameters and subject to interpretation on parameter counting or the “look elsewhere” effect (see [22] for a related study). Here we show that the tension is associated directly with the lensing effect on power spectra. Moreover, A_L will not be adequate in the future, when the CMB power spectra constrain more than just the amplitude of $C_L^{\phi\phi}$.

With the exception of $\Theta^{(1)}$, constraints on all the other parameters, i.e. the six Λ CDM parameters as determined from the data through their effect on the unlensed CMB, from Planck TT and SPT TEEE are mutually consistent; this is in agreement with findings of [40]. For example, we find that after marginalizing over $\Theta^{(i)}$, the constraint on the Hubble constant becomes $H_0 = (68.1 \pm 2.8)$ km/s/Mpc for SPT TEEE and (69.0 ± 1.2) km/s/Mpc for Planck TT.

To gain additional insight into the 3σ tension between SPT TEEE and Planck TT, in Fig. 8 we compare the constraints on $\Theta^{(1)}$ from these likelihoods as a function of the maximal ℓ_{\max} considered in the analysis. The tension is generated in the ℓ range between 1000 and 2000, with the two likelihoods pulling in the opposite directions. While the lensing constraining power of $\ell = 2000 - 3000$ in SPT TEEE is comparable to that of the $\ell \leq 2000$, there is no additional shift in $\Theta^{(1)}$.

In data space, the preference for high/low lensing shows as anomalously smooth/sharp acoustic peaks, which allows for a clear illustration of the tension. The $D_\ell^{XY} = \ell(\ell+1)C_\ell^{XY}/2\pi$ residuals between the SPT data and the best fit Λ CDM + 4 $\Theta^{(i)}$ model to the Planck TT data are shown in Figure 9. The residuals in C_ℓ^{EE} exhibit distinct oscillations in the ℓ range 1100-2200, with enhanced power at EE peaks and reduced at troughs, consistent with a deficit in lensing. Note that the TT

^{*8} There is a typo in [40], and the claimed 2.9σ tension should be 2.4σ .

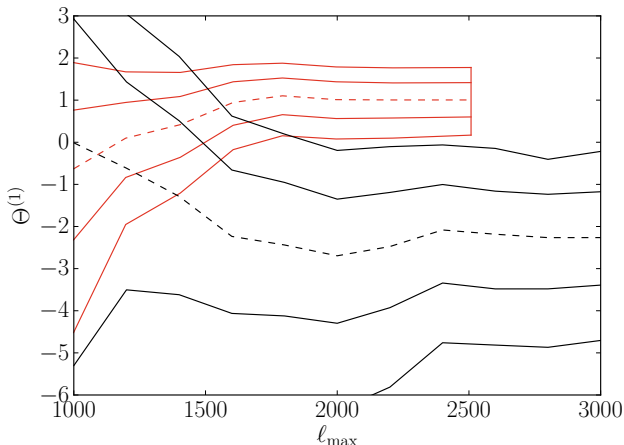


FIG. 8. Constraints on $\Theta^{(1)}$ from SPT TEEE (black) and Planck TT (red) likelihoods when only part of the data up to the maximal multipole ℓ_{\max} is used. The dashed lines show maximum likelihood values and the solid lines mark 68% and 95% confidence intervals.

peaks are out of phase with EE so that the smoothing in Planck TT and sharpening in SPT EE data occur at different multipoles, which makes this discrepancy difficult to explain with any physical mechanism.

VI. DISCUSSION

In the first part of this work, we use simulated lensed CMB data to perform the first investigation of covariances between and within TT , TE and EE power spectra measured by experiments observing a small patch of the sky. We find that in general the lensing-induced covariances are well described by a sum of the super-sample covariance, parameterizing effects of lenses larger than the footprint, and intra-sample lensing covariance, parameterizing effects of the smaller lenses.

As detailed in Appendix A 1, the amplitude of the ILC portion of the covariance is consistent with theoretical expectations whereas the SSC portion is about 5% larger in our simulations than theoretically expected. For a typical analysis, this discrepancy does not have any important consequence – at most it would increase the measurement errors on the angular extent of the sound horizon θ_* by the same amount in cases when SSC limits such measurements, i.e for small footprints. In Appendix A 2, we confirm and refine these results, expanding on the method of [35] which empirically extracts smooth features from a noisy estimate of a correlation matrix, effectively decreasing the numerical noise due to a limited number of simulations. In this work we use it to extract the SSC and ILC terms, ignoring terms close to the (sub)diagonals where the Gaussian and window function effects dominate, but this method is applicable to any noisy estimate

of a covariance matrix.

Likewise, the method of treating SSC by introducing an auxiliary parameter in the window can be extended to treat the principal modes of any such covariance matrix. For example, while we have omitted an analysis of C_ℓ^{BB} here due to complications from removing the C_ℓ^{EE} contamination caused by intermixing due to the mask, this technique can be straightforwardly implemented by modeling lensing covariance as a set of extra parameters to marginalize over in the model for C_ℓ^{BB} . However, such an analysis requires a known prior expectation for the distribution of these parameters, which in practice requires first a resolution of lensing tensions in the current data.

Finally extra sharpening of the acoustic peaks related to missing peak smoothing by the super-sample lenses is not detectable in our suite of simulations and is constrained to be negligible even for cosmic variance limited experiments in the investigated range of survey footprints, $150 \text{ deg}^2 - 1000 \text{ deg}^2$.

In the second part of this work, we apply our lensing induced covariance analysis to South Pole Telescope measurements. We find that the South Pole Telescope polarization constraints [40] have reached the levels of precision where the lensing-induced covariance terms have to be included in the analysis. Starting with the current generation of the CMB experiments, these effects will thus have to become a standard part of CMB data likelihoods. We show how the non-Gaussian ILC effect can be added in an analytic way to a covariance matrix based on Gaussian CMB assumptions, for example from Gaussian realizations of the power spectra. When the covariance matrix is calculated using lensed CMB simulations, the lensing-induced covariance is automatically included. In this case, the technique of Appendix A 2 can be used to diminish the numerical noise.

Parameterizing the mean lensing convergence in the SPTpol field $\bar{\kappa}_{\text{SPTpol}}$ and modelling it explicitly, instead of including the super-sample lensing into the SSC covariance matrix, leads to identical results when considering the SPTpol results alone – a nearly 60% increase in the uncertainty on θ_* . When combined with Planck information on θ_* within the Λ CDM model, it enables us to constrain this parameter $\bar{\kappa}_{\text{SPTpol}}$ from the data. The SPT TEEE data hint at underdensity in the SPTpol region, which is in agreement with the convergence calculated directly from the Planck lensing map. Adding ILC within Λ CDM leads to approximately 10% increase of the error bars of $\Omega_c h^2$, which is the parameter for which the gravitational lensing information is the most important.

Using the technique from [28] and including both the SSC and ILC effects, we obtain direct constraints on gravitational lensing for the various South Pole Telescope likelihoods and compare them against the Planck satellite constraints [38]. Because of non-Gaussian posteriors, we generalize the standard “shift in the means” statistic to determine tensions between the individual data sets, see Appendix C. While the various constraints from SPT are mutually consistent, we confirm that the SPT data sets

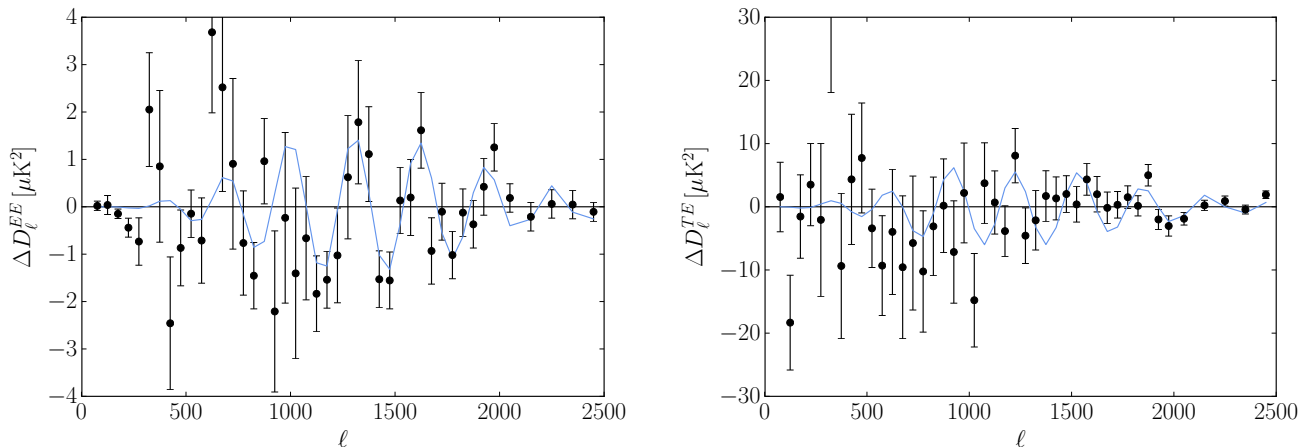


FIG. 9. Points show the difference between the SPT measured values of D_ℓ^{EE} (left) and D_ℓ^{TE} (right) and the best fit Λ CDM + 4 $\Theta^{(i)}$ model to the Planck TT. For comparison, in blue we show $-7 \times \partial C_\ell^{XY} / \partial \Theta^{(1)}$, binned with the same binning scheme.

prefer relatively low lensing power; the tension between SPT TEEE and Planck TT or Planck PP is significant at 3.0σ or 2.1σ respectively. Preference of SPT data for low lensing power was previously found in analyses based on the scaling parameter A_L [39, 40], however we find that when lensing tension between SPT TEEE and Planck TT is investigated using A_L , its significance is severely underestimated. Using the technique from [28] reveals the full lensing tension, and is thus recommended for comparing lensing constraints across various data sets. The inclusion of the ILC into the SPT TEEE likelihood strongly affects the probabilities to exceed the observed tensions. Had we not included it, the tensions between SPT TEEE and Planck constraints would grow by about 15%, reaching 3.5σ or 2.5σ between SPT TEEE and Planck TT or Planck PP respectively.

Constraints on $C_L^{\phi\phi}$ from ongoing and upcoming CMB experiments such as SPT 3G [15], Advanced ACT [16], Simons Observatory [18] and CMB-S4 [43] are expected to significantly improve the lensing constraints. The techniques developed in this work should prove even more important in quantifying and resolving these tensions in the future.

ACKNOWLEDGMENTS

We thank Tom Crawford, Jason Henning, Ue-Li Pen, Marco Raveri and Kimmy Wu for useful discussions. This work was supported by NASA ATP NNX15AK22G and the Kavli Institute for Cosmological Physics at the University of Chicago through grant NSF PHY-1125897 and an endowment from the Kavli Foundation and its founder Fred Kavli. WH was additionally supported by U.S. Dept. of Energy contract DE-FG02-13ER41958 and the Simons Foundation. We acknowledge use of the CAMB, Lenspix and CosmoMC software packages. This

work was completed in part with resources provided by the University of Chicago Research Computing Center.

Appendix A: Simulated vs. theoretical covariances

In this Appendix we quantify the agreement between the simulated covariance matrices $\text{Cov}_{bb'}^{XY,WZ}$ and their theoretical expectations. In the first part of the Appendix, we model the lensing-induced covariance as a sum of SSC and ILC terms with undetermined amplitudes and determine these amplitudes by minimizing the residuals versus the simulations. In the second part we present results based on an alternative quantification approach, expanding an eigenmode decomposition idea from [35], which empirically isolates the SSC and ILC effects.

1. Template fitting

In Fig. 10 we show the residuals between the correlation matrix $\hat{R}_{bb'}^{XY,WZ}$ obtained from simulations for the rectangular window function and the theoretical expectation used throughout the main text, $R_{(theory)bb'}^{XY,WZ}$. The residuals are small and appear noise-like, with the possible exception of $R^{TT,TT}$ at high ℓ which show hints of structure unrelated to the SSC or ILC template forms. As similar residuals do not appear for the other window functions considered here, indicating that it may be an artifact of the limited number of simulations, we do not investigate this issue further.

On the other hand, we can test the amplitude of the SSC and ILC effects considering their form as given. To do so, we look at the matrix elements away from the diagonals, where the Gaussian terms and window function effects are negligible. We focus on bins $|b - b'| > 2$ and

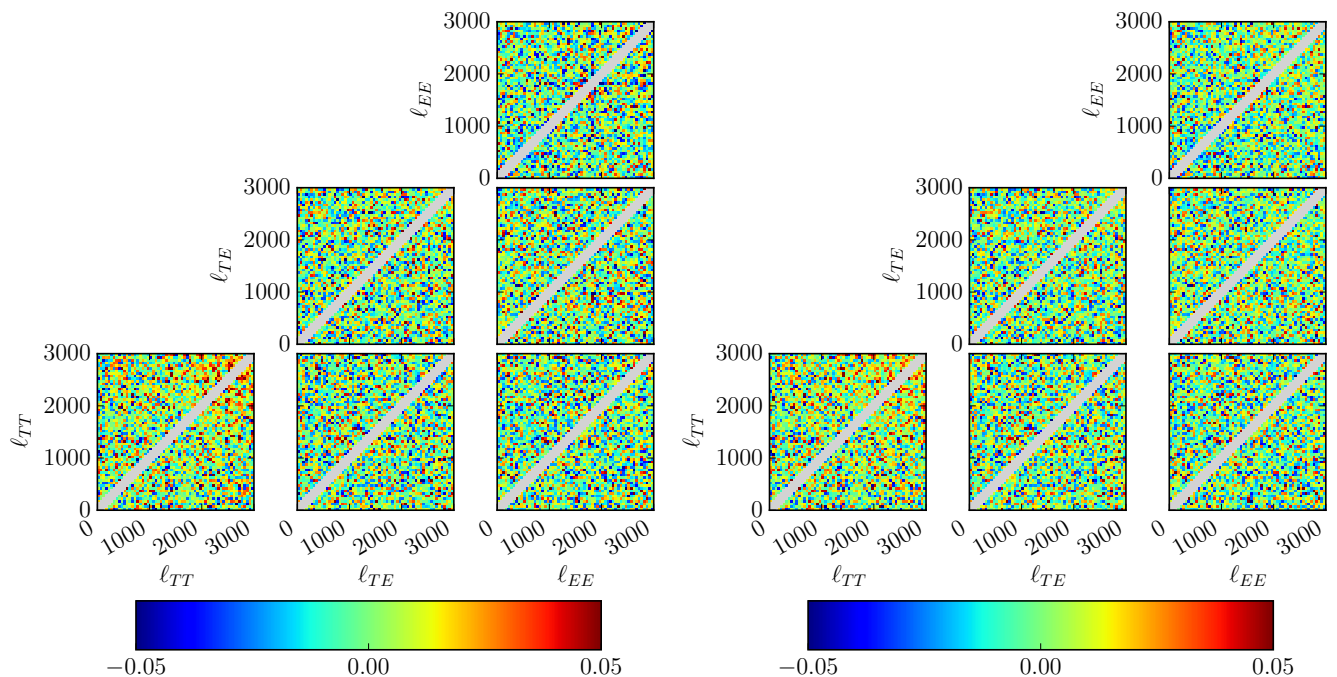


FIG. 10. Left: Residuals between the correlation matrix $\hat{R}_{bb'}^{XY,WZ}$ obtained from simulations and the theoretical expectation for the lensing-induced correlation with no rescaling of the SSC and ILC effects. Residuals are on a substantially smaller scale than the effects shown in Fig. 1 and are mainly consistent with noise (see text). The gray region hides elements dominated by Gaussian covariance terms and the window function effects. Right: Analogous residuals between the correlation matrix $\hat{R}_{bb'}^{XY,WZ}$ obtained from simulations and its approximation through (A6), again for the rectangular window function.

model the covariance there as

$$\text{Cov}_{(\text{model})bb'}^{XY,WZ} = A_1 \text{Cov}_{(\text{SSC})bb'}^{XY,WZ} + A_2 \text{Cov}_{(\text{ILC})bb'}^{XY,WZ} \quad (\text{A1})$$

with undetermined A_1, A_2 and construct the model correlation matrix $R_{(\text{model})bb'}^{XY,WZ}$ by generalizing (17).

We can quantify the level of agreement in the amplitudes by determining the values A_1, A_2 that minimize the residuals between the correlation matrix from simulations and the model,

$$\sum_{\substack{XY,WZ \\ |b-b'|>2}} \left(R_{(\text{model})bb'}^{XY,WZ} - \hat{R}_{bb'}^{XY,WZ} \right)^2, \quad (\text{A2})$$

and their uncertainties by bootstrap resampling with replacement from our 2400 simulations. We consider only multipoles up to $\ell = 3000$ in the minimization.

Allowing A_i to vary does not substantially decrease the residuals plotted in Fig. 10. The resulting values of A_i with the bootstrapped error bars are shown in Fig. 11 for all five window functions. While the ILC amplitudes are in good agreement with the theoretical expectation $A_2 = 1$, the SSC amplitudes show a clear positive bias. Due to super-sample lensing, the acoustic peaks thus shift around their fiducial positions slightly more than predicted by (14), though this does not have significant bearing on cosmological inferences, see §IV A.

One possible explanation of this discrepancy is complications arising from the edge effects, not considered in the derivation of (14).

2. Empirical determination of SSC, ILC modes

In this section we present an alternative method to assess how well the covariance matrix for the binned full sky power spectra \hat{C}_b^{XY} estimated from the simulations agree with the theoretical predictions of the lensing-induced effects.

The method extends the ideas presented in [35], where the aim was to parameterize features found in a correlation matrix R_{ij} obtained from an ensemble of simulations \hat{R}_{ij} and to decrease the numerical noise due to the finite number of simulations. The authors assumed that beyond the diagonal elements, which are equal to one by definition, the correlation matrix is relatively smooth. Their analysis proceeds as follows:

1. Initialize the $k = 0$ step by setting $R_{ij}^k = \hat{R}_{ij}$ for $i \neq j$ and $R_{ij}^k = 0$ for $i = j$.
2. Decompose R_{ij}^k into orthonormal eigenmodes as

$$R_{ij}^k = \sum_K \lambda_K^k v_{K,i}^k v_{K,j}^k. \quad (\text{A3})$$

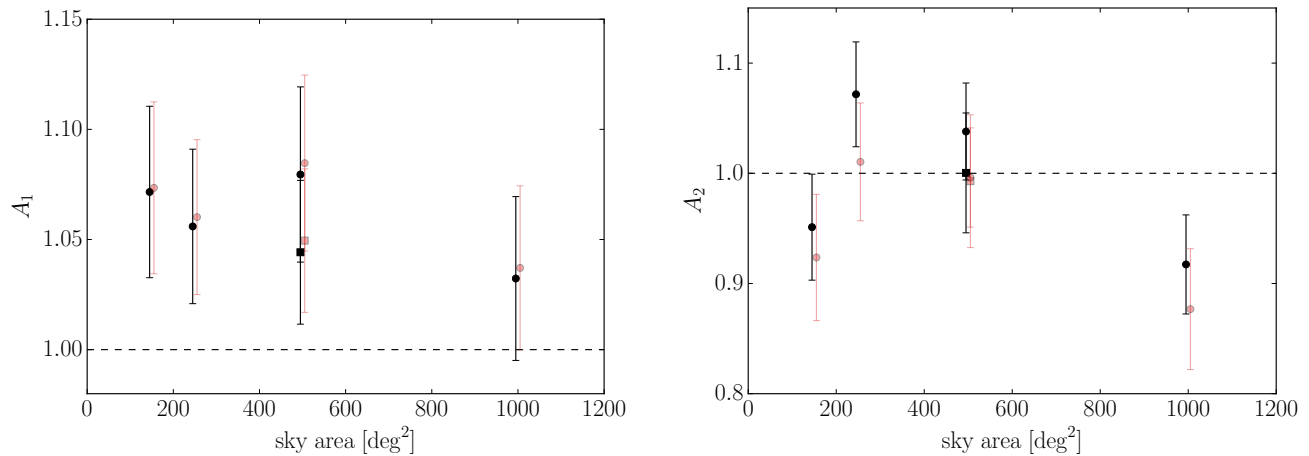


FIG. 11. Constraints on the amplitude parameters A_1, A_2 parameterizing the lensing induced covariance effects in the full covariance matrix (A1), as determined from the simulations. Black symbols represent values obtained by minimization of (A2), red symbols values obtained using the alternative method from the Appendix A2. Each point represents a different window function, the circles denote disk-shaped window functions and the squares the SPT-like rectangular window function. Error bars show 68% confidence limits obtained by bootstrapping. Theoretical expectations $A_i = 1$ are marked with the dashed line.

Examine the eigenvalues for a break in the spectrum and identify the N signal dominated modes (see below for an example).

3. Set $R_{ij}^{k+1} = \hat{R}_{ij}$ for $i \neq j$ and update its diagonal using the contribution of the N signal eigenmodes from step 2,

$$R_{ii}^{k+1} = \sum_{K=1}^N \lambda_K^k (v_{K,i}^k)^2. \quad (\text{A4})$$

4. Repeat steps 2 and 3 with $k \rightarrow k + 1$ until the elements on the diagonal converge to the required precision^{*9}.
5. Approximate the correlation matrix with the eigenvalues and eigenvectors of $R_{ij}^{k_{\max}}$ as

$$R_{ij} \approx \begin{cases} \sum_{K=1}^N \lambda_K^{k_{\max}} v_{K,i}^{k_{\max}} v_{K,j}^{k_{\max}} & i \neq j \\ 1 & i = j \end{cases}, \quad (\text{A5})$$

Because of the convergence of λ_K^k and $v_{K,i}^k$, the diagonal elements (A4) themselves converge and the estimate of the off-diagonal structure is not biased by the initial omission of the diagonal.

In our case, a similar procedure can be used with only a small alteration. Unlike in [35], in the correlation matrix

(12) there are features we are not interested in probing not only on the main diagonal $R_{bb}^{XY,XY}$, but due to Gaussian covariance terms also on the sub-diagonals $R_{bb}^{XY,WZ}$ and due to the window function effects also on the neighboring bins $R_{bb'}^{XY,WZ}$. In practice, we generalize the procedure by zeroing out the $b-2 \leq b' \leq b+2$ elements for all XY, WZ and replacing them with the iterative construction above. This is conservative as we only see evidence for window function effects in the nearest neighboring bin with the fiducial bin width and windows. With this procedure, we isolate the lensing-induced features of the correlation matrix.

In analyzing the simulated covariance matrices $\hat{R}_{bb'}^{XY,WZ}$ we find that with 2400 simulations we can only detect two features – the SSC and ILC effects. This is illustrated in Fig. 12, where we show distribution of converged eigenvalues λ_K for the 1000 deg^2 disk window when using $N = 2$ in the algorithm above. The two eigenvalues corresponding to SSC and ILC are clearly separated from the other eigenvalues. We infer that the others are too small to be detectable with 2400 simulations. When using other values of N , Fig. 12 or other results further below do not appreciably change, we thus quote results for $N = 2$ in what follows. The situation is identical for the other window functions.

For each window function, we use the iterative procedure to find vectors V_1, V_2 that approximate the lensing-induced structure of the correlation matrix as

$$R_{bb'}^{XY,WZ} \approx V_{1b}^{XY} V_{1b'}^{WZ} + V_{2b}^{XY} V_{2b'}^{WZ} \quad (|b - b'| > 2). \quad (\text{A6})$$

These vectors are related to the expansion (A5) through

$$V_{Kb}^{XY} = \sqrt{\lambda_K^{k_{\max}}} v_{Kb}^{k_{\max}, XY}. \quad (\text{A7})$$

^{*9} For the covariance matrices investigated in this work we find that relative error on $\lambda_K^k, v_{K,i}^k$ for $K = 1, 2$ drops by about a factor of three with each additional iteration. We performed 15 iterations for each covariance matrix.

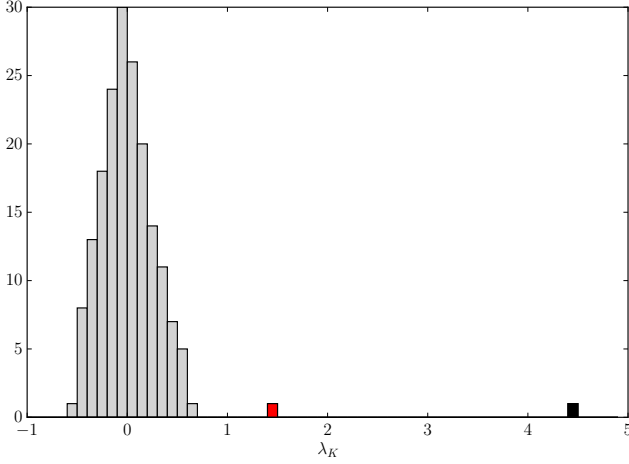


FIG. 12. Distribution of eigenvalues λ_K obtained from the simulated covariance for the 1000 deg² disk window using the method described in Appendix A 2. The eigenvalue corresponding to the SSC effect is colored in black, while the one corresponding to the ILC effect in red. The other eigenvalues arise from numerical noise and potentially other features of the covariance matrix that are not distinguishable with 2400 simulations.

In Fig. 10, we compare the residuals between the simulations and (A6) (right) with those between the simulations and the theory from the previous section (left). The residuals for the two approaches are qualitatively similar with a slightly higher residuals for the latter as would be expected from a theoretical as opposed to phenomenological model.

We can gain further insight about the relationship between the first two eigenmodes $V_{1,2}^{XY}$ and the theoretical expectations of the SSC and ILC effects by examining eigenvectors of the latter. From (13) we see the contribution of the SSC term to the correlation matrix can be factored into

$$\frac{\text{Cov}_{(\text{SSC})bb'}^{XY,WZ}}{\sqrt{\text{Cov}_{bb}^{XY,XY} \text{Cov}_{b'b'}^{WZ,WZ}}} = U_{1b}^{XY} U_{1b'}^{WZ} \quad (\text{A8})$$

with

$$U_{1b}^{XY} = \sum_{\ell} \frac{u_{b\ell}^{XY}}{\sqrt{\text{Cov}_{bb}^{XY,XY}}} \frac{\partial \ell^2 C_{\ell}^{XY}}{\partial \ln \ell} \frac{\sigma_{\kappa}}{\ell^2}. \quad (\text{A9})$$

The ILC covariance including only TT, TE and EE is well captured by a single eigenvector [21]. Its contribution to the correlation matrix can be then well approximated by

$$\frac{\text{Cov}_{(\text{ILC})bb'}^{XY,WZ}}{\sqrt{\text{Cov}_{bb}^{XY,XY} \text{Cov}_{b'b'}^{WZ,WZ}}} \approx U_{2b}^{XY} U_{2b'}^{WZ} \quad (\text{A10})$$

for some U_{2b}^{WZ} that can be obtained using eigenvalue decomposition. Because the leading lensing principal component $\Theta^{(1)}$ captures most of the lensing effect, U_2^{XY} can

be well approximated by

$$U_{2b}^{XY} \approx \sum_{\ell} \frac{u_{b\ell}^{XY}}{\sqrt{\text{Cov}_{bb}^{XY,XY}}} \frac{\partial C_{\ell}^{XY}}{\partial \Theta^{(1)}} \sigma_{\Theta^{(1)}}^A, \quad (\text{A11})$$

where $\sigma_{\Theta^{(1)}}^A$ is the sample variance of $\Theta^{(1)}$ in the footprint (24). We checked (A11) explicitly, but use the numerically obtained value U_2^{XY} in what follows.

If the theoretical predictions for ILC and SSC are correct, we expect

$$V_{Kb}^{XY} \approx U_{Kb}^{XY}, \quad K = 1, 2. \quad (\text{A12})$$

In Figure 13 we compare these two vectors and find that the agreement is indeed very good, confirming in a different way that our theoretical understanding of the lensing-induced terms in the simulated covariance matrix is satisfactory.

Similarly to before, we can introduce amplitudes $A'_{1,2}$ to quantify agreement between V_{Kb}^{XY} and U_{Kb}^{XY} and estimate their values by minimizing

$$\sum_{XY,b} \left(V_{1b}^{XY} - \sqrt{A'_1} U_{1b}^{XY} \right)^2 \quad (\text{A13})$$

and similarly for A'_2 . The square root is used so that in an ideal case, where the two techniques for comparing simulated and theoretical covariance matrices produce identical results, we would get $A_K = A'_K$. We can estimate uncertainties on $A'_{1,2}$ again using bootstrap. The results are plotted in Fig. 11, where they can be compared against results of the method introduced in the Appendix A 1. The difference between the two methods is much smaller than the uncertainties for the amplitude of the SSC term A_1 , but there seem to be a small bias for A_2 , with the method presented in this section obtaining smaller values.

Resolution of this issue could lie in the relative detection significance of these two effects. From Fig. 12 it is clear that the SSC effect is detected with a higher significance and that the eigenvalue corresponding to the ILC effect is notably closer to the noise-fitting eigenvalues clustered around zero. Our hypothesis is that V_2 obtained from the simulations contains an admixture of the noisy modes. This then leads to misalignment of V_2 and U_2 , and a decrease in A'_2 . This hypothesis is corroborated by the fact that the agreement between the two methods of obtaining A_2 improves when we drop the temperature data, where the ILC signal is relatively weaker. Additionally, the difference between the two methods increases when the analysis is repeated with a smaller number of simulations, in which case we expect larger admixture of the noisy modes into V_2 .

Overall, the differences in the amplitudes A_i of ILC and SSC determined from simulations from the theoretical expectation of unity are small and so in the main text we simply set $A_i = 1$.

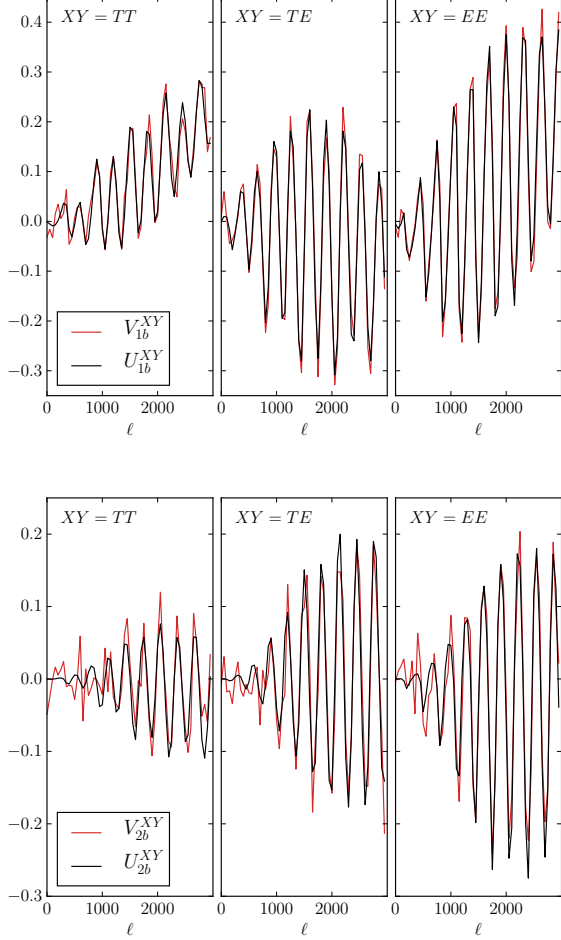


FIG. 13. The two leading scaled eigenmodes V_{Kb}^{XY} (for $K = 1, 2$) determined from the simulated covariance matrix using the method of Appendix A 2 (red) against the theoretical expectations (black). The top plot shows agreement for the SSC effect, while the lower for the ILC effect. Simulated results were obtained for the 1000 deg² disk window function.

Appendix B: Sharpening of windowed peaks

As explained in the main text, we expect cut sky power spectra to exhibit sharper peaks than the full sky power spectra, because lenses larger than the survey footprint do not average out to cause peak smoothing, but act as a coherent (de)magnification. Since this is also the sense in which the SPT data are in tension with Planck, in this Appendix we demonstrate that it cannot reduce the tension.

To do that, we compare the unbiased estimates of the binned power spectra \hat{C}_b^{XY} against the theoretically expected value $U_{b\ell}^{XY} C_\ell^{XY}$. Here C_ℓ^{XY} are the theoretically predicted full sky power spectra for our fiducial cosmological model. If the amount of lensing in \hat{C}_b^{XY} is indeed smaller, it should be possible to detect nonzero $\Theta^{(1)}$ in

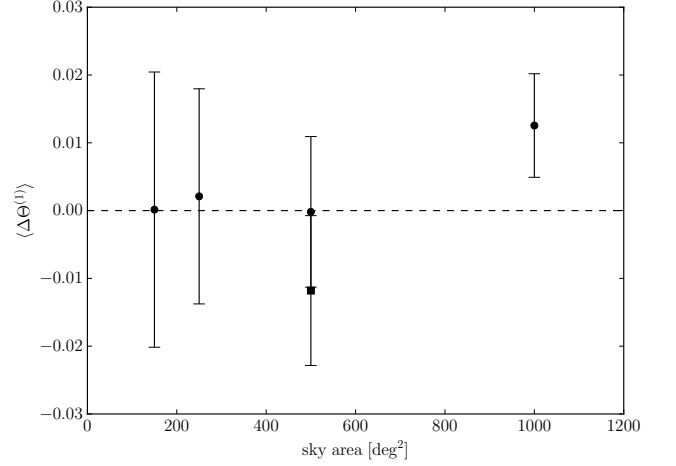


FIG. 14. Constraints on extra sharpening of the peaks in cut-sky simulations, studied in Appendix B. Each point represents a different window function, the circles denote disk-shaped window functions and the square the SPT-like rectangular window function. For each window, the central value represents a mean of the 2400 values of $\Delta\Theta^{(1)}$ obtained from our simulations. The error bars represent error on this mean, standard deviation of the $\Delta\Theta^{(1)}$ distribution divided by $\sqrt{2400}$.

the difference

$$\Delta C_b^{XY} = \hat{C}_b^{XY} - \sum_{\ell} U_{b\ell}^{XY} C_{\ell}^{XY}. \quad (\text{B1})$$

We model this difference as

$$\Delta C_{(\text{model})b}^{XY} = \sum_{\ell} U_{b\ell}^{XY} \left(\Delta\Theta^{(1)} \frac{\partial C_{\ell}^{XY}}{\partial \Theta^{(1)}} + \Delta\theta_* \frac{\partial C_{\ell}^{XY}}{\partial \theta_*} \right), \quad (\text{B2})$$

to account for the two effects lensing has on power spectra in a cut sky experiment.

From the simulated ΔC_b^{XY} we then constrain $\Delta\Theta^{(1)}, \Delta\theta_*$ for each simulation and each window function by minimizing

$$\sum_{\substack{XY, WZ \\ bb'}} \Delta_b^{XY} \left(\text{Cov}_{bb'}^{XY, WZ} \right)^{-1} \Delta_{b'}^{WZ}, \quad (\text{B3})$$

where the residuals are

$$\Delta_b^{XY} = \Delta C_b^{XY} - \Delta C_{(\text{model})b}^{XY}; \quad (\text{B4})$$

this minimization can be done algebraically. For each window we can then read off mean values of $\Delta\Theta^{(1)}$ and $\Delta\theta_*$ and their variance from the obtained distribution.

As expected, mean shift of the peaks $\langle \Delta\theta_* \rangle$ is consistent with zero. So is the mean shift in $\langle \Delta\Theta^{(1)} \rangle$ that quantifies the extra sharpening of the peaks; in Fig. 14 we show constraints on $\langle \Delta\Theta^{(1)} \rangle$ for all the window functions considered in this work. Even though on theoretical grounds the sharpening of the peaks is expected to be

present, our simulations limit the magnitude of this effect to be a small fraction of the $\Theta^{(1)}$ standard deviation due to lens sample variance (24), i.e. $|\langle \Delta\Theta^{(1)} \rangle| \ll \sigma_{\Theta^{(1)}}^A$.

Appendix C: Tension significance for non-Gaussian posteriors

Determining the level of agreement between two measurements of a variable x is an often encountered problem. The approximation usually employed is to assume independence of these measurements and approximate the corresponding posterior probability densities $P_1(x), P_2(x)$ as two Gaussians with means μ_i and variances σ_i^2 . The tension in the units of the total variance σ is then calculated using the difference of the means formula

$$T = \frac{|\mu_1 - \mu_2|}{\sqrt{\sigma_1^2 + \sigma_2^2}}. \quad (\text{C1})$$

In the case where the two posteriors are not Gaussian, it may be possible to apply a nonlinear transformation of the variable x , after which the posteriors are better approximated by Gaussians. This was the path taken for example in [38]. Finding such a transformation can

be time consuming and may not be always possible. For that reason we introduce here a tension statistic that can be directly used in the general case.

Let us assume the two measurements are in principle correlated and described by the posterior probability density $P(x_1, x_2)$, where x_1, x_2 label results of the two measurements. For such P we evaluate

$$\begin{aligned} \mathcal{P}(2 > 1) &= \int_0^\infty d\Delta \int P(x, x + \Delta) dx \\ \mathcal{P}(1 > 2) &= \int_{-\infty}^0 d\Delta \int P(x, x + \Delta) dx \\ &= 1 - \mathcal{P}(2 > 1) \end{aligned} \quad (\text{C2})$$

and calculate T from

$$\min[\mathcal{P}(2 > 1), \mathcal{P}(1 > 2)] = \int_T^\infty \frac{dx}{\sqrt{2\pi}} e^{-x^2/2}. \quad (\text{C3})$$

The tension significance is then marked as $T\sigma$.

For the special case where P factorizes into two independent Gaussians this definition is equivalent to the standard formula (C1). Additionally, this tension significance is invariant with respect to reparameterizations of the measured variable x .

-
- [1] D. N. Spergel *et al.* (WMAP), *Astrophys. J. Suppl.* **148**, 175 (2003), arXiv:astro-ph/0302209 [astro-ph].
- [2] R. Adam *et al.* (Planck), (2015), arXiv:1502.01582 [astro-ph.CO].
- [3] A. Lewis and A. Challinor, *Phys. Rept.* **429**, 1 (2006), arXiv:astro-ph/0601594 [astro-ph].
- [4] K. M. Smith, O. Zahn, and O. Dore, *Phys. Rev. D* **76**, 043510 (2007), arXiv:0705.3980 [astro-ph].
- [5] C. M. Hirata, S. Ho, N. Padmanabhan, U. Seljak, and N. A. Bahcall, *Phys. Rev. D* **78**, 043520 (2008).
- [6] D. Hanson *et al.* (SPTpol), *Phys. Rev. Lett.* **111**, 141301 (2013), arXiv:1307.5830 [astro-ph.CO].
- [7] S. Das *et al.*, *Phys. Rev. Lett.* **107**, 021301 (2011), arXiv:1103.2124 [astro-ph.CO].
- [8] R. Keisler *et al.*, *Astrophys. J.* **743**, 28 (2011), arXiv:1105.3182 [astro-ph.CO].
- [9] P. A. R. Ade *et al.* (The Planck Collaboration), *Astron. & Astrophys.* **571**, A17 (2014), arXiv:1303.5077.
- [10] R. Keisler *et al.* (SPT), *Astrophys. J.* **807**, 151 (2015), arXiv:1503.02315 [astro-ph.CO].
- [11] P. A. R. Ade *et al.* (Planck), *Astron. Astrophys.* **594**, A15 (2016), arXiv:1502.01591 [astro-ph.CO].
- [12] P. A. R. Ade *et al.* (BICEP2, Keck Array), (2016), arXiv:1606.01968 [astro-ph.CO].
- [13] B. D. Sherwin *et al.*, *Phys. Rev. D* **95**, 123529 (2017), arXiv:1611.09753 [astro-ph.CO].
- [14] N. Aghanim *et al.* (Planck), (2018), arXiv:1807.06210 [astro-ph.CO].
- [15] B. A. Benson *et al.* (SPT-3G), *Proceedings, SPIE Astronomical Telescopes + Instrumentation 2014: Millimeter, Submillimeter, and Far-Infrared Detectors and Instrumentation for Astronomy VII: Montreal, Quebec, Canada, June 24-27, 2014*, Proc. SPIE Int. Soc. Opt. Eng. **9153**, 91531P (2014), arXiv:1407.2973 [astro-ph.IM].
- [16] S. W. Henderson *et al.*, *Proceedings, 16th International Workshop on Low Temperature Detectors (LTD 16): Grenoble, France, July 20-24, 2015*, J. Low. Temp. Phys. **184**, 772 (2016), arXiv:1510.02809 [astro-ph.IM].
- [17] W. L. K. Wu *et al.*, *Proceedings, 16th International Workshop on Low Temperature Detectors (LTD 16): Grenoble, France, July 20-24, 2015*, J. Low. Temp. Phys. **184**, 765 (2016), arXiv:1601.00125 [astro-ph.IM].
- [18] J. Aguirre *et al.* (Simons Observatory), (2018), arXiv:1808.07445 [astro-ph.CO].
- [19] A. Benoit-Lvy, K. M. Smith, and W. Hu, *Phys. Rev. D* **86**, 123008 (2012), arXiv:1205.0474 [astro-ph.CO].
- [20] A. Manzotti, W. Hu, and A. Benoit-Lvy, *Phys. Rev. D* **90**, 023003 (2014), arXiv:1401.7992 [astro-ph.CO].
- [21] J. Peloton, M. Schmittfull, A. Lewis, J. Carron, and O. Zahn, (2016), arXiv:1611.01446 [astro-ph.CO].
- [22] M. Raveri and W. Hu, (2018), arXiv:1806.04649 [astro-ph.CO].
- [23] A. G. Riess, S. Casertano, W. Yuan, L. Macri, J. Anderson, J. W. MacKenty, J. B. Bowers, K. I. Clubb, A. V. Filippenko, D. O. Jones, and B. E. Tucker, *Astrophys. J.* **855**, 136 (2018), arXiv:1801.01120 [astro-ph.SR].
- [24] F. Khlinger *et al.*, *Mon. Not. Roy. Astron. Soc.* **471**, 4412 (2017), arXiv:1706.02892 [astro-ph.CO].
- [25] P. A. R. Ade *et al.* (Planck), *Astron. Astrophys.* **594**, A13 (2016), arXiv:1502.01589 [astro-ph.CO].
- [26] N. Aghanim *et al.* (Planck), *Astron. Astrophys.* **607**, A95

- (2017), arXiv:1608.02487 [astro-ph.CO].
- [27] G. E. Addison, Y. Huang, D. J. Watts, C. L. Bennett, M. Halpern, G. Hinshaw, and J. L. Weiland, *Astrophys. J.* **818**, 132 (2016), arXiv:1511.00055 [astro-ph.CO].
- [28] P. Motloch, W. Hu, and A. Benoit-Lévy, *Phys. Rev. D* **95**, 043518 (2017), arXiv:1612.05637 [astro-ph.CO].
- [29] P. Motloch and W. Hu, *Phys. Rev. D* **96**, 103517 (2017), arXiv:1709.03599 [astro-ph.CO].
- [30] A. Lewis, *Phys. Rev. D* **71**, 083008 (2005), arXiv:astro-ph/0502469 [astro-ph].
- [31] A. Lewis, A. Challinor, and A. Lasenby, *Astrophys. J.* **538**, 473 (2000), arXiv:astro-ph/9911177 [astro-ph].
- [32] R. Adam *et al.* (Planck), *Astron. Astrophys.* **596**, A108 (2016), arXiv:1605.03507 [astro-ph.CO].
- [33] E. Hivon, K. M. Gorski, C. B. Netterfield, B. P. Crill, S. Prunet, and F. Hansen, *Astrophys. J.* **567**, 2 (2002), arXiv:astro-ph/0105302 [astro-ph].
- [34] M. L. Brown, P. G. Castro, and A. N. Taylor, *Mon. Not. Roy. Astron. Soc.* **360**, 1262 (2005), arXiv:astro-ph/0410394 [astro-ph].
- [35] J. Harnois-Deraps and U.-L. Pen, *Mon. Not. Roy. Astron. Soc.* **423**, 2288 (2012), arXiv:1109.5746 [astro-ph.CO].
- [36] N. Aghanim *et al.* (Planck), *Astron. Astrophys.* **594**, A11 (2016), arXiv:1507.02704 [astro-ph.CO].
- [37] N. Aghanim *et al.* (Planck), (2018), arXiv:1807.06209 [astro-ph.CO].
- [38] P. Motloch and W. Hu, *Phys. Rev. D* **97**, 103536 (2018), arXiv:1803.11526 [astro-ph.CO].
- [39] G. Simard *et al.* (SPT), Submitted to: *Astrophys. J.* (2017), arXiv:1712.07541 [astro-ph.CO].
- [40] J. W. Henning *et al.* (SPT), *Astrophys. J.* **852**, 97 (2018), arXiv:1707.09353 [astro-ph.CO].
- [41] A. Lewis and S. Bridle, *Phys. Rev. D* **66**, 103511 (2002), arXiv:astro-ph/0205436 [astro-ph].
- [42] A. Gelman and D. B. Rubin, *Statist. Sci.* **7**, 457 (1992).
- [43] K. N. Abazajian *et al.* (CMB-S4), (2016), arXiv:1610.02743 [astro-ph.CO].